

# Damage Identification in Aging Aircraft Structures with Piezoelectric Wafer Active Sensors

VICTOR GIURGIUTIU,\* ANDREI ZAGRAI AND JINGJING BAO

*University of South Carolina, Columbia, SC 29208, USA*

**ABSTRACT:** Piezoelectric wafer active sensors can be applied to aging aircraft structures to monitor the onset and progress of structural damage such as fatigue cracks and corrosion. Two main detection strategies are considered: (a) the wave propagation method for far-field damage detection; and (b) the electro-mechanical (E/M) impedance method for near-field damage detection. These methods are developed and verified on simple-geometry specimens, and then tested on realistic aging-aircraft panels with seeded cracks and corrosion. The specimens instrumentation with piezoelectric-wafer active sensors and ancillary apparatus is presented. The experimental methods, signal processing, and damage detection algorithms, tuned to the specific method used for structural interrogation, are discussed. In the wave propagation approach, the pulse-echo and acousto-ultrasonic methods were considered. Reflections from seeded cracks were successfully recorded. In addition, acoustic emission and low-velocity impact were also detected. In the E/M impedance method approach, the high-frequency spectrum is processed using overall-statistics damage metrics. The  $(1-R^2)^3$  damage metric, where  $R$  is the correlation coefficient, was found to yield the best results. The simultaneous use of the E/M impedance method in the near field and of the wave propagation method in the far field opens the way for a comprehensive multifunctional damage detection system for aging aircraft structural health monitoring.

*Key Words:* structural health monitoring, damage detection, embedded ultrasonics, electro-mechanical impedance method, piezoelectric wafer active sensors, PWAS, EMI, Lamb waves, guided waves, impedance, diagnostics, structural health monitoring, aging aircraft

## INTRODUCTION

### Aircraft Structural Health Monitoring

KEGAMI and Haugse (2001) showed that Integrated Vehicle Health Management (IVHM) reduces total life cycle cost and increases safety and availability of military and commercial aircraft. Although the incorporation of IVHM systems can lead to higher initial acquisition cost, the eventual savings in operation and support costs will far outweigh the initial investment. Structural Health Management System (SHMS) architecture for the aging military aircraft fleet require rapid assessment of damage location, damage extent, and damage severity. The Durability Patch Program for high-cycle-fatigue crack-damage repair uses technologies for patch integrity assessment based on both conventional strain gauges and novel piezoelectric active sensors (Stanford University's "smart layer"). The latter uses through-transmission acousto-ultrasonic methods based on elastic wave signals send and received by piezoelectric active sensors. In another application,

broadband acoustic emission is used to detect crack initiation and crack propagation through the reception of the elastic waves send in the structure from the advancing crack tip. For commercial aircraft, NASA's Aviation Safety Program considers a large-scale deployment of conventional strain sensors interlinked through wireless communication.

For the aircraft of the future, Goldin et al. (2001) envisioned the concept of an entire wing surface covered with tiny embedded sensors and actuators. Like the nerves of a bird, the sensors would monitor and analyze temperatures, pressures, and vibrations. Across the entire vehicle, intelligent systems composed of sensors, actuators, microprocessors, and adaptive controls would provide a full-system distributed-knowledge network, the central nervous system to command and control the adaptive physical response.

Mal (2001) discussed an Intelligent Structural Health Monitoring System (ISHMS) for the nondestructive evaluation (NDE) of aircraft and aerospace structures, which consists of attached or embedded acoustic emission sensor arrays and signal processing/interpretation methodology. Experiments performed on fatigue coupon specimens using conventional acoustic emission equipment showed the detection of extensional and

\*Author to whom correspondence should be addressed.  
E-mail: victorg@sc.edu

flexural Lamb waves emanating from the advancing crack tip. Data processing consisting of signal filtering, and joint time–frequency analysis such as Short Time Fourier Transform (STFT) and Wigner-Ville Distribution (WVD), wavelet transforms, and Choi-Williams distribution were discussed. Farrar et al. (2001) discussed the integrated structural health monitoring system consisting of sensors, actuator, microprocessor, and wireless communication.

### Piezoelectric Wafer Active Sensors

Piezo-electric active sensors are small, nonintrusive, inexpensive piezoelectric wafers that are intimately affixed to the structure and can actively interrogate the structure (Giurgiutiu and Zagari, 2002). Piezoelectric active sensors are nonresonant devices with wide band capabilities. They can be wired into sensor arrays and connected to data concentrators and wireless communicators. Piezoelectric active sensors have captured the interest of both academia and industry (Chang, 1995, 1988, 2001; Bartkiewicz et al., 1996; Boller et al., 1999) because of their low cost, small invasiveness, and dual-action (emission and reception) capability. The general constitutive equations of linear piezoelectric materials given by ANSI/IEEE Standard 176-1987, describe a tensorial relation between mechanical and electrical variables (mechanical strain,  $S_{ij}$ ; mechanical stress,  $T_{kl}$ ; electrical field,  $E_k$ , and electrical displacement  $D_j$ ) in the form:

$$\begin{aligned} S_{ij} &= s_{ijkl}^E T_{kl} + d_{kij} E_k \\ D_j &= d_{jkl} T_{kl} + \varepsilon_{jk}^T E_k \end{aligned} \quad (1)$$

where  $s_{ijkl}^E$  is the mechanical compliance of the material measured at zero electric field ( $E=0$ ),  $\varepsilon_{jk}^T$  is the dielectric permittivity measured at zero mechanical stress ( $T=0$ ), and  $d_{kij}$  is the piezoelectric coupling between the electrical and mechanical variables. Figure 1(a) shows an active sensor consisting of a Lead Zirconate Titanate (PZT) piezoceramic wafer affixed to the structural surface. In this configuration, mechanical stress and strain are applied in the 1 and 2 directions, i.e. in the plane of the surface, while the electric field acts in the 3 direction, i.e., normal to the surface. Hence, the significant electro-mechanical couplings for this type of analysis are the 31 and 32 effects. The application of an electric field,  $E_3$ , induces surface strains,  $S_{11}$  and  $S_{22}$ , and vice-versa. As the PZT sensor is activated, interaction forces and moments appear (Figure 1(b)):

$$M_a = F_{PZT} \frac{h}{2}, \quad F_{PZT} = \hat{F}_{PZT} e^{i\omega t}, \quad N_a = F_{PZT} \quad (2)$$

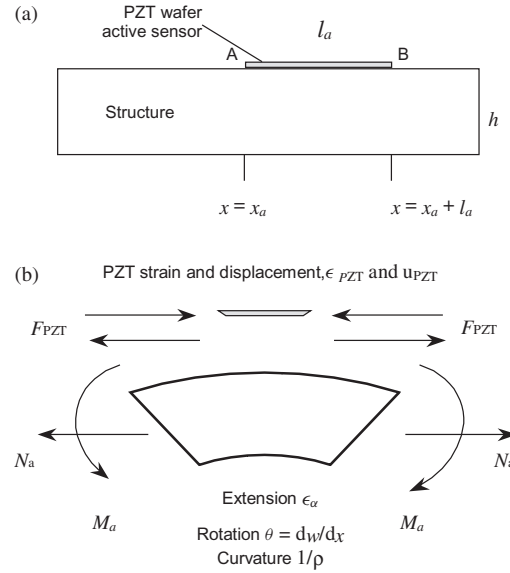


**Figure 1.** Piezoelectric active sensor interaction with host structure: (a) PZT wafer affixed to the host structure; (b) Interaction forces and moments.

### The Present Investigation

The present investigation set forth to investigate the capability of piezoelectric-wafer active sensors to perform damage detection in aging aircraft structures. One of the major objectives of this investigation was to prove that this new class of sensors could perform the same functions as the conventional ultrasonic transducer and acoustic emission sensors, while being much cheaper and less obtrusive. To this end, we studied the adaptation of ultrasonic and acousto-ultrasonic methods, which were devised for conventional ultrasonic transducers. In particular, we investigated the use of guided Lamb wave methods, which offer special advantages for damage detection in large-area thin-wall structures. We also proved that detection of simulated acoustic emission signals, and of low-velocity impacts, is also possible using an array of piezoelectric-wafer active sensors. Another major objective of this investigation was to explore new damage detection concepts that are unique to the use of piezoelectric-wafer active sensors. To this end, the electro-mechanical (E/M) impedance method was studied, explored, and verified.

In our investigation we used two types of specimens: (a) simple geometry specimens for methods calibration and validation; and (b) realistic aircraft panels containing simulated crack and corrosion damage representative of aging-aircraft structures. The aging aircraft panels were constructed at Sandia National Labs using aircraft construction technology (Figure 2). Each specimen features a lap splice joint, tear straps, and hat-shaped stringer/stiffeners. The whole construction is made of 1 mm (0.040") 2024-T3 Al-clad sheet assembled with 4.2 mm (0.166") diameter countersunk

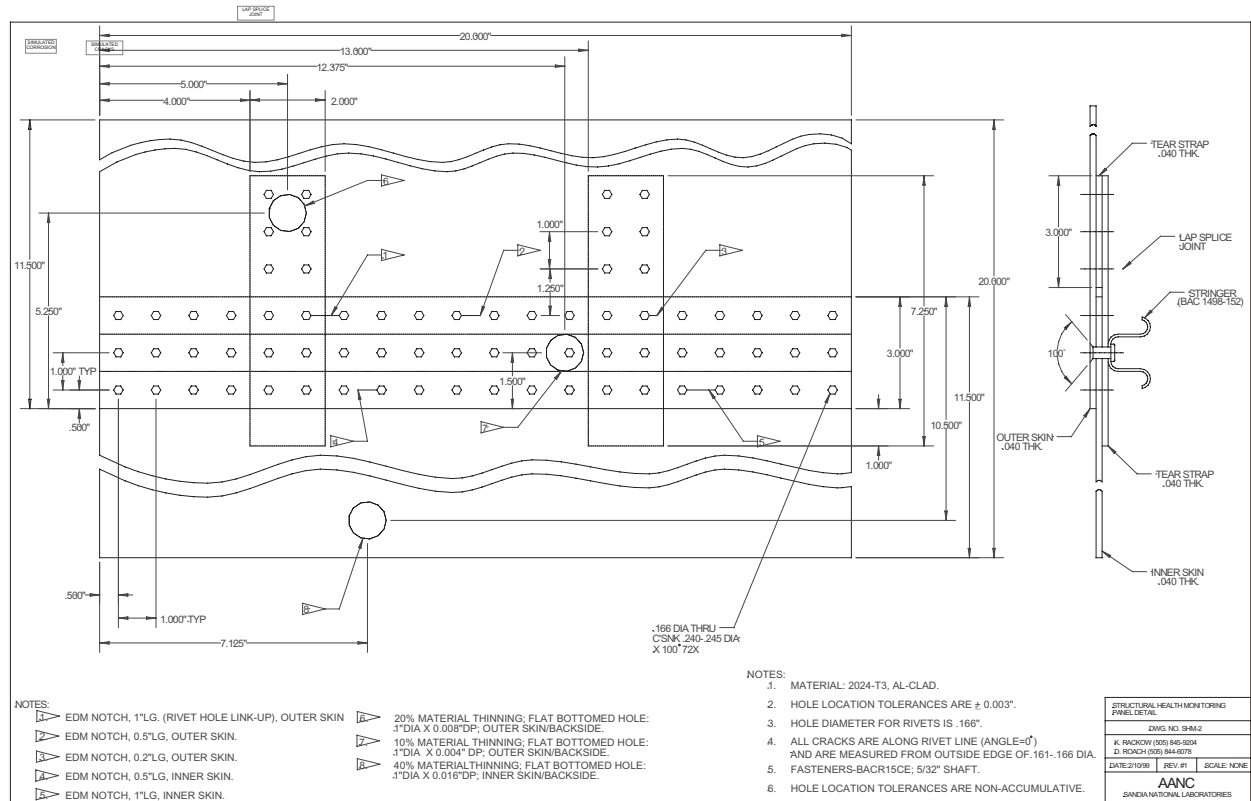


Figure 2. Realistic aging aircraft lap-splice joint panel with simulated cracks (EDM slits) and corrosion (chem-mill areas).

rivets. Cracks were simulated using the Electric Discharge Machining (EDM) process and consisted of hairline through-the-thickness slits of various lengths (5–25 mm). Corrosion damage was simulated using the chemical milling (Chem.-Milled) process by removing between 10 and 40% of the material thickness from several 25.4 mm diameter areas, as detailed in Figure 2. Three specimens were provided: (1) pristine; (2) with cracks only; (3) with corrosion only. The specimens were instrumented with piezoelectric active sensors consisting of 0.2 mm thick APC-850 PZT wafers, silver electrodes on both sides, from American Piezoceramics Corporation. The specimen instrumentation and experimental measurements were performed in the Laboratory for Adaptive Materials and Smart Structures of the Department of Mechanical Engineering of the University of South Carolina.

## GUIDED PLATE WAVES (LAMB WAVES) DAMAGE IDENTIFICATION

Lamb waves, or plate waves, are ultrasonic elastic waves that travel inside and along thin plates. Lamb waves can propagate in two modes, symmetric (S) and antisymmetric (A). The wave velocity depends on the product of frequency and material thickness.

Investigations of Lamb and leaky Lamb waves have been pursued theoretically and experimentally for a variety of applications, ranging from seismology, to ship construction industry, to acoustic microscopy, and to nondestructive testing and acoustic emission (Krautkramer and Krautkramer, 1990; Rose, 1999; Lemistre et al., 1999).

Rose (2001) outlined the inspection potential of ultrasonic guided wave for the detection of cracks, delaminations, and disbonds, and gave examples utilizing conventional angle-probe ultrasonic transducers. Light et al. (2001) studied the detection of defects in thin steel plates using ultrasonic guided Lamb waves and conventional ultrasonic equipment. De Villa et al. (2001) presented results of defect detection in thin plates using  $S_0$  Lamb wave scanning. Conventional ultrasonic equipment consisting of wedge transmitter and bubbler receiver mounted on a scanning arm was utilized. Signal processing methods for the determination of the arrival times and of the flaw location were explored. Flaw localization results for simulated cracks (notches) with various sizes (from 2 to 3.5 in.) and different inclinations (from 0 to 45°) were presented.

A comprehensive description of the Lamb-wave theory and analysis can be found in Viktorov (1967) and Rose (1999). The Lamb wave speed is obtained by solving the Rayleigh–Lamb equation. First, define

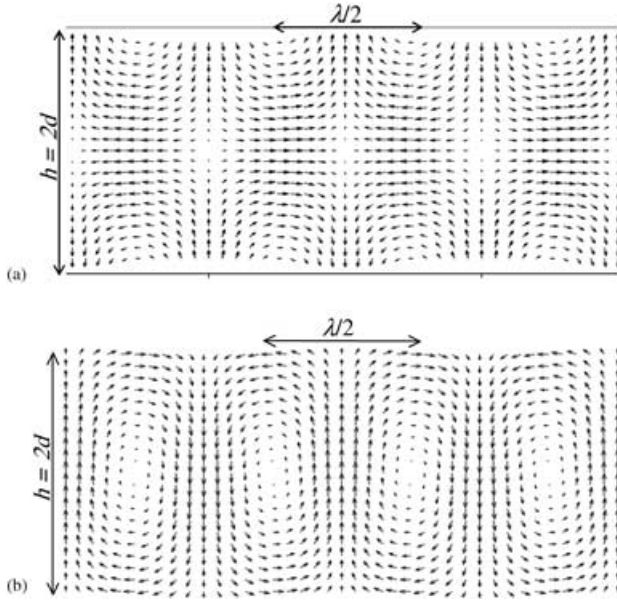


**Figure 3.** Simulation of lamb waves in a 1-mm thick aluminum plate: (a) Symmetric mode  $S_0$ ,  $f=1.56$  MHz; (b) Antisymmetric mode  $A_0$ ,  $f=0.788$  MHz. For full animation, see <http://www.engr.sc.edu/research/lamss/default.htm> under research Thrust 1.

$\xi = \sqrt{c_S^2/c_P^2}$ ,  $\zeta = \sqrt{c_S^2/c_L^2}$ , and  $\bar{d} = k_S d$ ; where  $c_L$  is the Lamb wave speed, and  $d$  is the half thickness of the plate. In addition, also define Lamb wave number  $k_L = \omega/c_L$ , and the variables,  $q = \sqrt{k_L^2 - k_P^2}$ ,  $s = \sqrt{k_L^2 - k_S^2}$ . For symmetric motion (Figure 3(a)), the Rayleigh–Lamb frequency equation

$$\frac{\tan(\sqrt{1 - \zeta^2} \bar{d})}{\tan \sqrt{\xi^2 - \zeta^2}} + \frac{4\zeta^2 \sqrt{1 - \zeta^2} \sqrt{\xi^2 - \zeta^2}}{(2\zeta^2 - 1)^2} = 0 \quad (3)$$

yields the value of  $\zeta$ . Hence, one can write the two components of the particle motion, as plotted in Figure 3(a):

$$\begin{aligned} U(x, z, t) &= \text{Re} \left[ A k_L \left( \frac{\cosh(qz)}{\sinh(qd)} - \frac{2qs}{k_L^2 + s^2} \frac{\cosh(sz)}{\sinh(sd)} \right) e^{i(k_L x - \omega t \frac{\omega}{2})} \right] \end{aligned} \quad (4)$$

$$\begin{aligned} W(x, z, t) &= \text{Re} \left[ A q \left( \frac{\sinh(qz)}{\sinh(qd)} - \frac{2k_L^2}{k_L^2 + s^2} \frac{\sinh(sz)}{\sinh(sd)} \right) e^{i(k_L x - \omega t)} \right] \end{aligned} \quad (5)$$

For antisymmetric motion (Figure 3(b)), similar equations can be derived.

Figure 4 presents the dispersive (frequency dependant) symmetric and antisymmetric ( $S_0$  and  $A_0$ ) Lamb

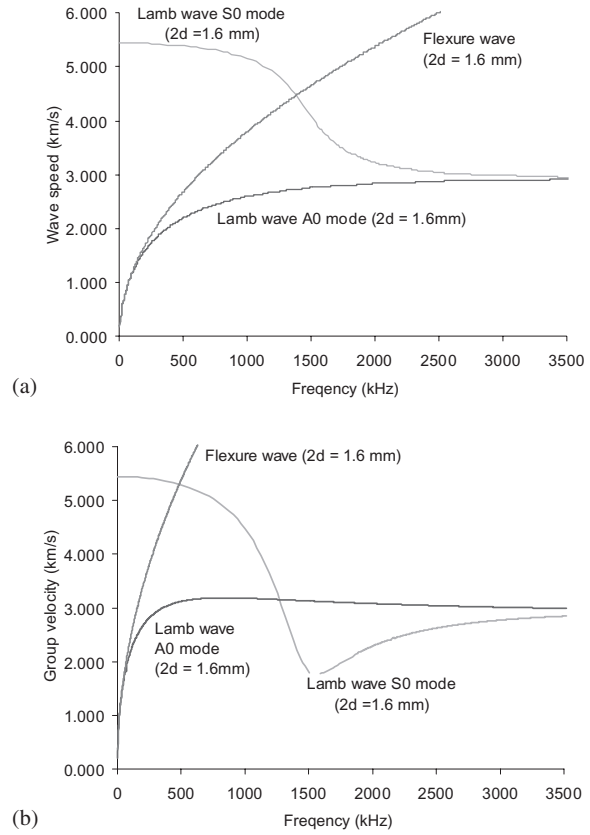


**Figure 4.** Dispersion curves in 1.6 mm aluminum plates: (a) Wave speed; (b) Group velocity.

wave speed and group velocity in 1.6-mm aluminum plates (Giurgiutiu et al., 2001). Also shown in Figure 4 are the conventional (Bernoulli-Euler) flexural waves. One notices that, at low frequencies, the conventional flexural wave and the  $A_0$  Lamb wave speeds tend to coincide. At high frequencies, the Lamb wave speed reaches a horizontal asymptote, while the flexural wave speed would continue to increase.

### Lamb Wave Experiments on Rectangular Plates

To understand and calibrate the Lamb-waves damage-detection method, active-sensor experiments were conducted on thin metallic plates of regular geometries (Giurgiutiu et al., 2001). A 1.6 mm thick, 2024-aluminum alloy plate (914 mm  $\times$  504 mm) was instrumented with an array of eleven 7 mm  $\times$  7 mm PZT wafer active sensors positioned on a rectangular grid (Table 1). The sensors were connected with thin insulated wires to a 16-channel signal bus and two 8-pin connectors (Figure 5). An HP33120A arbitrary signal generator was used to generate a smoothed 300 kHz tone-burst excitation with a 10 Hz repetition rate. The signal was sent to active sensor #11, which generated a package of elastic waves that spread out into the entire plate. A Tektronix TDS210 two-channel digital

**Table 1. Locations of sensors on the thin rectangular plate specimen.**

Sensor #	1	2	3	4	5	6	7	8	9	10	11
x (mm)	100	100	100	100	100	450	450	450	800	800	800
y (mm)	100	175	250	325	400	100	250	400	100	250	400

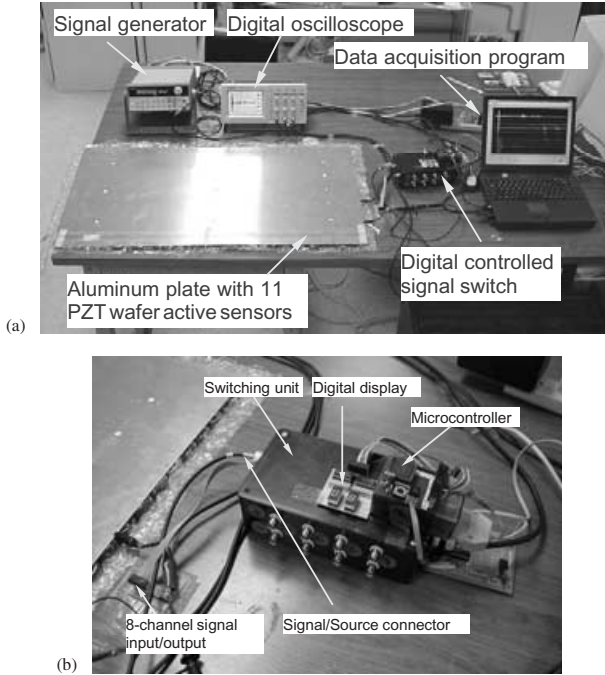


**Figure 5. Experimental setup for rectangular plate wave propagation experiment: (a) Overall view showing the plate, active sensors, and instrumentation; (b) Detail of the microcontroller and switch box.**

oscilloscope, synchronized with the signal generator, was used to collect the signals captured at the remaining 10 active sensors. A digitally controlled switching unit and a LabView data acquisition program were used. A Motorola MC68HC11 microcontroller was tested as an embedded stand-alone option. These systematic experiments gave conclusive results regarding the feasibility of exciting elastic wave in aircraft-grade metallic plates using small inexpensive and unobtrusive piezoelectric-wafer active sensors:

- (a) Excitation and reception of high-frequency Lamb waves was verified over a large frequency range (10–600 kHz). For axial,  $S_0$ , waves, an excitation “sweet spot” was found at around 300 kHz (Figure 6(a)).
- (b) The elastic waves generated by this method had remarkable clarity and showed a 99.99% distance–time correlation. The group velocity correlated very well with the theoretical predictions (Figure 6(b)).
- (c) The pulse-echo method was successfully verified using the active sensor #11 in a dual role: (i) to generate elastic waves (“initial bang”); and (ii) to

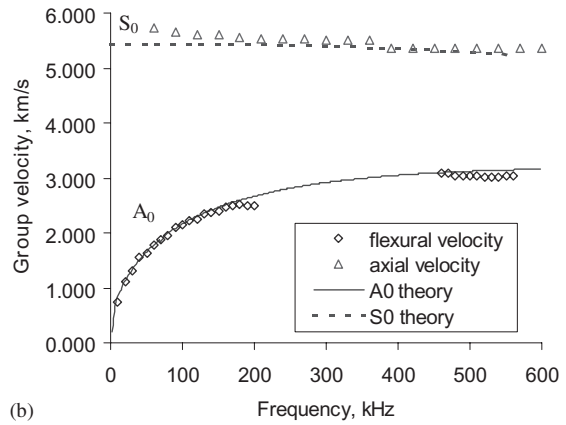
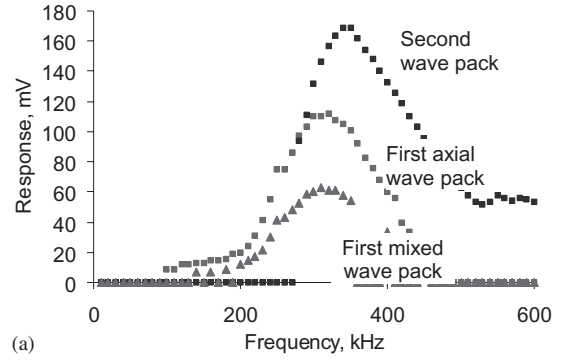


**Figure 6. (a) Frequency tuning studies identified a maximum wave response around 300 kHz; (b) Group velocity dispersion curves for Lamb-wave  $A_0$  and  $S_0$  modes.**

**Table 2. Analysis of pulse-echo signals of sensor #11 on rectangular plate specimen.**

Wave Pack Label	$R_1$	$R_2$	$R_3$	$R_4$	$R_5$	$R_6$	$R_7$	$R_8$
Time of flight ( $\mu$ s)	43.8	48.8	152.8	194.4	233.2	302.8	343.2	380.8
Path length (mm)	104	114	400	504	608	800	914	1008

capture the echo signals of the waves reflected by the plate boundaries and coming back to the transmitter sensor (Table 2 and Figure 7). Very good correlation was obtained ( $R^2 = 99.99\%$ ).

**Lamb Wave Experiments on Aging-aircraft Panel**

Lamb-wave active-sensor damage detection strategy stems from the ultrasonic and acousto-ultrasonic damage-detection methodologies (Blitz and Simpson, 1996; Duke, 1988, respectively). Wave propagation experiments were conducted on the aging aircraft panels of Figure 2 using a number of PZT active sensors affixed at various locations. Several experiments

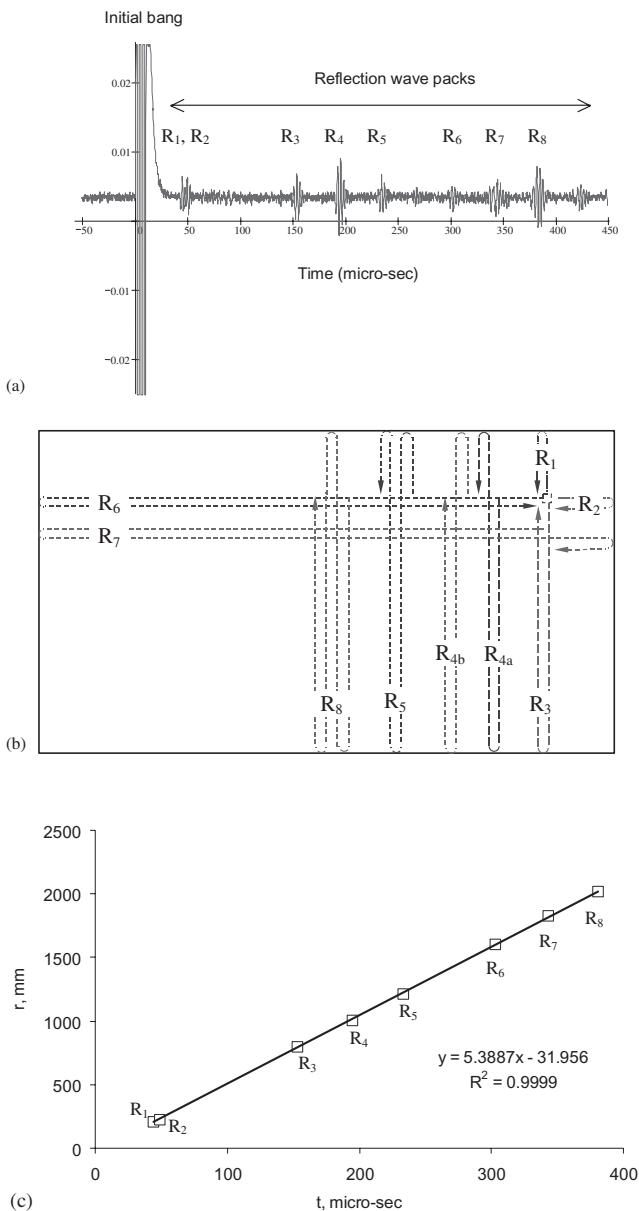


**Figure 7.** Pulse-echo method applied to active sensor #11: (a) The excitation signal and the echo signals on active sensor 11; (b) Schematic of the wave paths for each wave pack; (c) Correlation between path length and time of flight ( $R^2 = 99.99\%$ ).

were performed to verify the wave propagation properties, and to identify the reflections due to the intrinsic construction features of the panels (rivets, splice joints, etc.) Damage detection of cracks and corrosion damage was studied and verified. For illustration, Figures 8 and 9 present a crack detection example. Figure 8 shows three photographs of piezoelectric wafer active sensor installation on increasingly more complex structural regions. The most complex situation is presented in Figure 8(c), which shows a vertical row of splice rivets in the far left, a horizontal double row of stiffener rivets in the middle, and a simulated crack (12.75 mm EDM hairline slit) starting from the

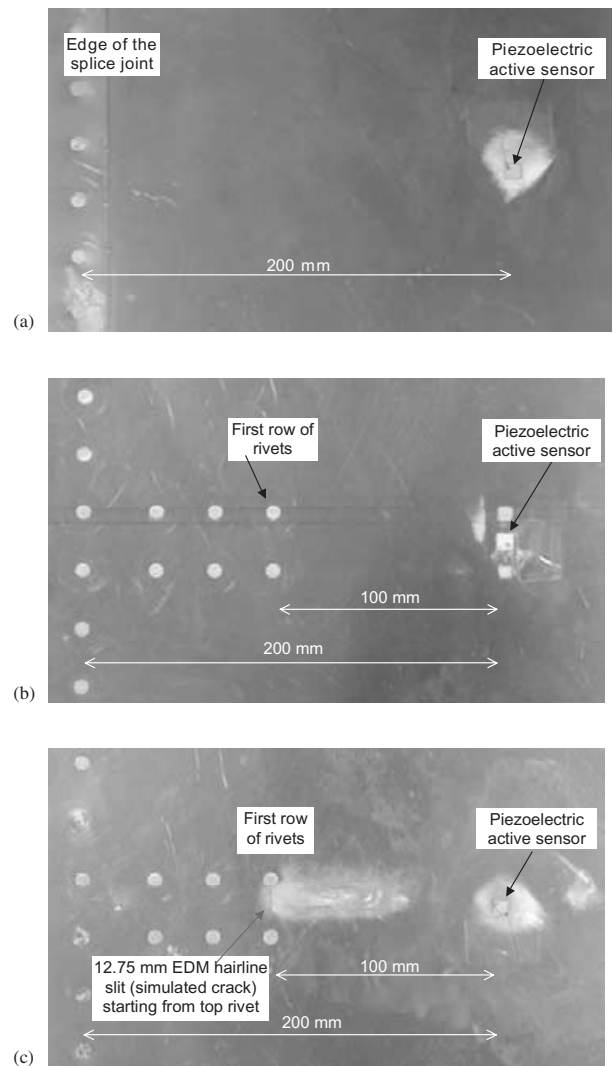


**Figure 8.** Crack detection experiment on aging aircraft panel: (a) Pristine panel featuring an active sensor placed in a rivet-free region; (b) Pristine panel featuring an active sensor placed at 100 mm from a row of rivets; (c) Damaged panel featuring a 12.75 mm EDM hairline slit (simulated crack) starting from the top rivet.

right-most rivet of the top row horizontal. This photo represents the damaged specimen. Figure 8(b) shows the same area on the pristine specimen. No crack is present. Otherwise, the structural features are identical to those of Figure 8(c). Figure 8(a) shows the situation with the lowest complexity, in which only the vertical row of rivets is present in the far left. On all three panels, a piezoelectric active sensor was placed in the same location, i.e., at 200 mm from the vertical row of rivets, i.e., at 100 mm from the start of the horizontal row of rivets. Consistent with the pulse-echo methods, the sensors were used for both excitation and reception.

Figure 9 shows the analysis of the signals recorded during this experiment. Figure 9(a) shows the signal recorded on the pristine panel in a region without rivets. It features the initial bang (centered at around 5.3  $\mu$ s) and multiple reflections from the panel edges. The

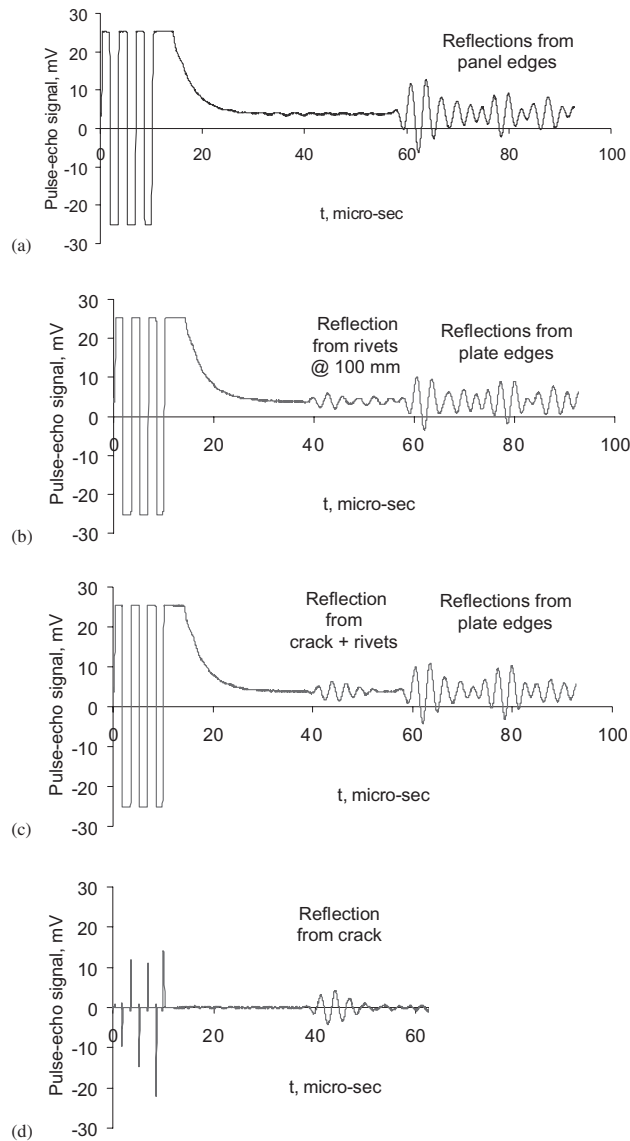


**Figure 9.** Analysis of the pulse-echo signals during the crack detection experiment: (a) Signal recorded on the pristine panel featuring the reflection from the rivet and from the panel edges; (b) Signal recorded on the cracked panel featuring, in addition, the reflections due to the presence of the crack; (c) Difference in signals indicating a strong reflection presence of crack.

reflections start to arrive at approximately  $60 \mu\text{s}$ . Figure 9(b) shows the signal recorded on the pristine panel, which has horizontal rivets starting at 100 mm from the sensor. The signal features the reflections from the rivets in addition to the multiple reflections from the panel edges. The reflection from the rivets arrives at approximately  $42 \mu\text{s}$ , indicating an approximate time-of-flight having the value  $\text{TOF} = 37 \mu\text{s}$ . This TOF is consistent with traveling 200 mm at a  $S_0$  group velocity of approximately 5.4 km/s (c.f., Figure 6(b)). Figure 9(c) shows the signal recorded on the damaged panel. It shows features similar to those of Figure 9(b), but somehow stronger at the  $42 \mu\text{s}$  position. These features correspond to reflection from the rivets, the reflections

from panel edges, and the crack. By subtracting the signal of Figure 9(b) from that of Figure 9(c), the effect of the presence of the crack could be unambiguously identified. The result of this subtraction is shown in Figure 9(d). A strong wave pack centered on  $42 \mu\text{s}$ , labeled “reflection from the crack” is featured. The cleanness of the crack detection feature and the quietness of the signal ahead of the crack detection feature are remarkable. Thus, we concluded that this method permits a clean and unambiguous detection of structural cracks. An array of active sensors can be used in a round-robin fashion to generate and detect elastic waves that interrogate the aging aircraft structure in order to determine the presence of cracks and corrosion.

### Acoustic Emission Detection with Piezoelectric Wafer Active Sensors

Historically, acoustic emission signals have been captured with special-purpose acoustic emission sensors (e.g., Dzenis and Qian, 2001; Ikegami and Haugse, 2001; Mal, 2001), which are costly and obtrusive. Blanas et al. (1997) and Dupont et al. (2000) studied the possibility of using embedded piezoelectric wafer sensors to detect acoustic emission signals in composite materials. To prove the capability of PZT wafer active sensors to detect acoustic emission signals in metallic materials, we performed detection experiments on the rectangular plate specimen, which was already instrumented with the array of 11 PZT-wafer active sensors (Table 1). Acoustic emission events were simulated at the location  $P$ ,  $x_P = 400 \text{ mm}$ ,  $y_P = 200 \text{ mm}$  (Figure 10(a)). Table 3 shows the location of the sensors and their radial distance from the AE event. Consistent with other investigators, (e.g., Blanas et al., 1997; Dzenis and Qian, 2001), the acoustic emission events were simulated by pencil lead breaks on the specimen surface (0.5 mm HB leads). The simulated acoustic emission signals captured at sensors #1, #5, #7, #9 are shown in Figure 10(b) (for display, the signals were spaced up by DC shifts). The signal on sensor #7, closest to the AE source ( $r_7 = 71 \text{ mm}$ ), is the strongest. This signal displays both high-frequency and low-frequency components, corresponding to  $S_0$  (axial) and  $A_0$  (flexural) waves, respectively. The flexural ( $A_0$ ) waves display much higher amplitudes than the axial ( $S_0$ ) waves, though their travel speed is slower. The signals received at the other sensors display similar trends, though of lower amplitudes, due to their greater distance from the AE source. These experiments have proven that the piezoelectric-wafer active sensors are capable of detecting AE signals. The high sensitivity of these sensors is remarkable: signals of up to  $\pm 0.5 \text{ V}$  were directly recorded without the need for any signal conditioning/pre-amplifiers.

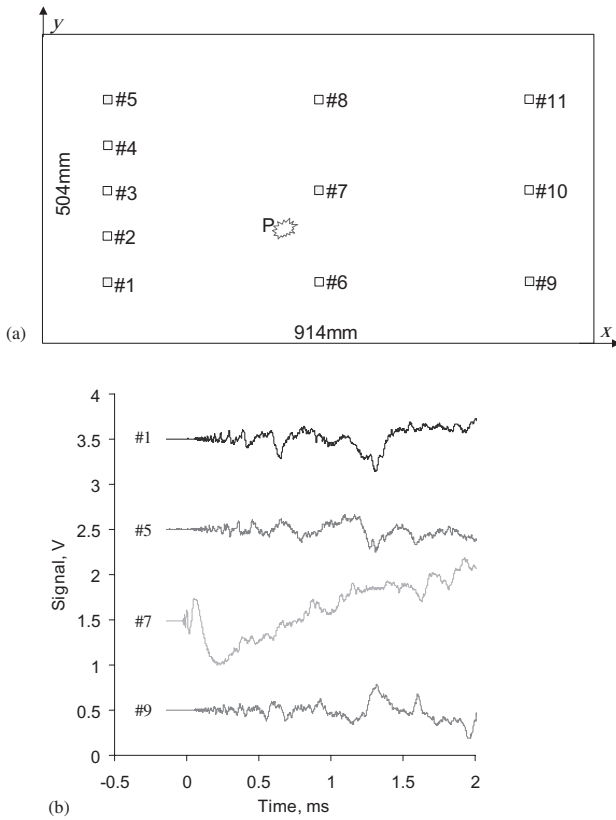


**Figure 10.** Acoustic emission (AE) experiments: (a) Location of sensors and simulated AE event,  $P$  ( $x_P=400$  mm,  $y_P=200$  mm); (b) Captured AE signals. The AE event was a 0.5 mm pencil lead break; the locations of the sensors and of the event are given in Table 3.

**Table 3.** Position of sensors ( $x$ ,  $y$ ) and their radial distance,  $r$ , from the acoustic emission (AE) and impact detection (ID) events. The TOF was adjusted by  $73 \mu\text{s}$  to account for oscilloscope trigger effects.

Sensor	Distance (mm)			TOF for ID ( $\mu\text{s}$ )	
	$x$	$y$	$r$	Raw	Adjusted
#1	100	100	316	120	193
#5	100	400	361	156	229
#7	450	250	71	-31	42
#9	800	100	412	180	253
AE/ID event	400	200	0	N/A	N/A

### Impact Detection with Piezoelectric Wafer Active Sensors

Impact detection with piezoelectric wafer active sensors in composite materials was successfully demonstrated by Wang and Chang (2000). In our experiments, we used the array of piezoelectric wafer active sensors was also used to detect low-velocity foreign object impact on metallic aircraft-grade aluminum plates. In our experiments, we used a small steel ball (0.16 g) dropped from a height of 50 mm. Figure 11(a) presents the signals recorded on sensors #1, #5, #7, #9. The corresponding TOF values are

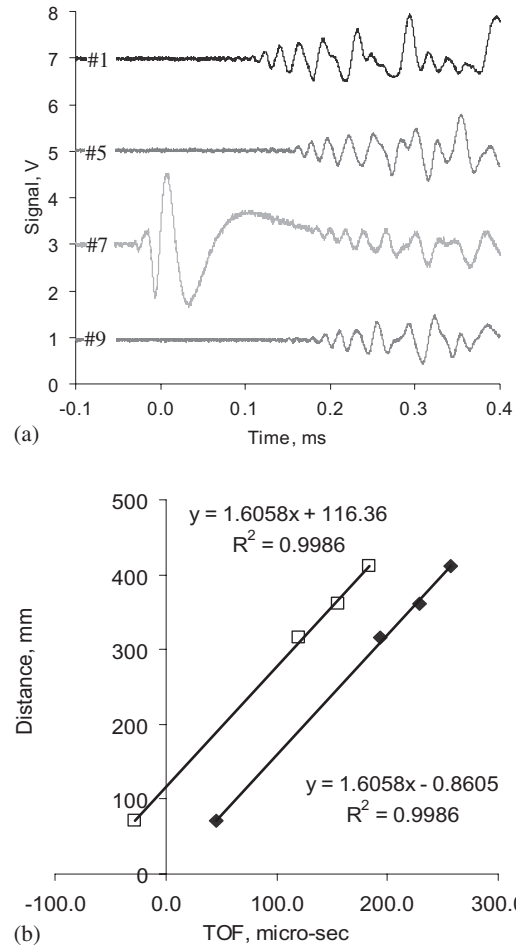


**Figure 11.** Impact detection (ID) experiments: (a) Captured ID signals; (b) Straight-line fit of the distance-TOF values (top = raw time data; bottom = adjusted for Oscilloscope trigger). The ID event was a 0.16 g steel-ball dropped from a 50 mm height; the locations of the sensors and of the event are given in Table 3.

$t_1 = 0.1070$  ms,  $t_5 = 0.1560$  ms,  $t_7 = -0.0312$  ms,  $t_9 = 0.1800$  ms, relative to the oscilloscope trigger. Figure 11(b) shows the straight line fit through the distance-TOF points. The top line represents the raw data: a group velocity of  $c = 1.6058$  km/s is determined from the straight-line gradient (99.86% correlation). This group velocity is consistent with the predicted  $A_0$  group velocity value corresponding to basic signal frequency of 45 kHz (c.f., Figure 6(b)). The bottom line of Figure 11(b) represents the distance-TOF correlation obtained after the TOF was adjusted for the Oscilloscope trigger response ( $\Delta\text{TOF} = 73 \mu\text{s}$ ). This line passes through the origin, as expected.

The distance and TOF data (Table 3) was used to detect the impact position. Assuming the unknown impact position is  $(x, y)$ , the following set of simultaneous nonlinear equations represent the correlation between distance, group velocity, and TOF:

$$(x_i - x)^2 + (y_i - y)^2 = (c \cdot t_i)^2, \quad i = 1, \dots, 4 \quad (6)$$

These equations represent an over-constrained set of (equations (4 equations, 2 unknowns)), which can be solved using error minimization routines. In our studies, we tried two methods: (a) global error minimization; and (b) individual error minimization. It was found that individual error minimization gave marginally better results. The impact location determined by these calculations was  $x_{\text{impact}} = 400.7$  mm,  $y_{\text{impact}} = 187.5$  mm. These values are within 0.2 and 6.2%, respectively, of the actual impact location (400 and 200 mm).

These experiments have proven that the piezoelectric-wafer active sensors are capable of detecting low-velocity impact signals. The high sensitivity of these sensors is remarkable: signals of up to  $\pm 1.5$  V were directly recorded without the need for any signal conditioning/pre-amplifiers. It was also shown how data processing algorithms can determine the impact location with reasonable accuracy.

## ELECTRO-MECHANICAL IMPEDANCE DAMAGE IDENTIFICATION

The impedance method is a damage detection technique complementary to the wave propagation techniques. Ultrasonic equipment manufacturers offer, as an option, mechanical impedance analysis (MIA) probes and equipment (Staveley NDT Technologies, 1998). The mechanical impedance method consists of exciting vibrations of bonded plates using a specialized transducer that simultaneously measures the applied normal force and the induced velocity. Cawley (1984) extended Lange's (1978) work on the mechanical impedance method and studied the identification of local disbonds in adhesively bonded plates using a small shaker. Though phase information was not used in Cawley's analysis, present-day MIA methodology uses both magnitude and phase information to detect damage.

The electro-mechanical (E/M) impedance method (Giurgiutiu and Rogers, 1997; Giurgiutiu and Zagrai, 2002) is an emerging technology that uses in-plane surface excitation to measure the pointwise mechanical impedance of the structure through the real part of the electrical impedance measured at the sensor terminals. The measured impedance parameters such as real and imaginary parts, amplitude, phase, etc. serve as potential indicators of structural damage. The principles of the E/M impedance technique are illustrated in Figure 12(a). The drive-point impedance presented by the structure to the active sensor can be expressed as the frequency dependent variable,  $Z_{\text{str}}(\omega) = k_{\text{str}}(\omega) / i\omega = k_e(\omega) - \omega^2 m(\omega) + i\omega c_e(\omega)$ . Through the mechanical coupling between the PZT active sensor and the host structure, on one hand, and through the electro-

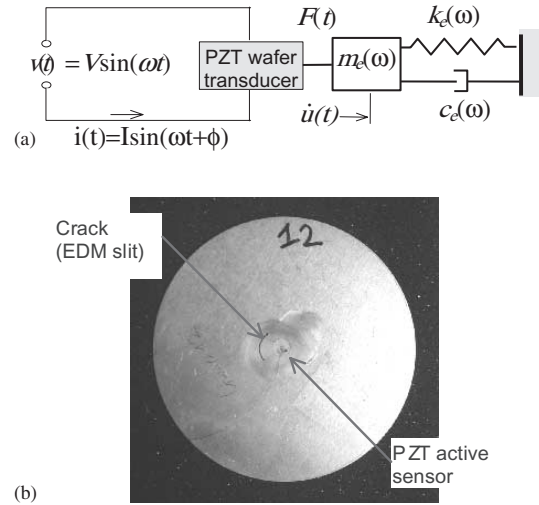


**Figure 12.** (a) Electro-mechanical coupling between PZT active sensor and structure; (b) Thin circular plate with a 7-mm diameter piezoelectric-wafer active sensor at its center.

mechanical (E/M) transduction inside the PZT active sensor, on the other hand, the drive-point structural impedance is reflected directly in the electrical impedance,  $Z(\omega)$ , at the active sensor terminals:

$$Z(\omega) = \left[ i\omega C \left( 1 - \kappa_{31}^2 \frac{\chi(\omega)}{1 + \chi(\omega)} \right) \right]^{-1}, \quad (7)$$

where  $C$  is the zero-load capacitance of the PZT active sensor and  $\kappa_{31}$  is the electro-mechanical cross coupling coefficient of the PZT active sensor ( $\kappa_{31} = d_{13} / \sqrt{s_{11} \epsilon_{33}}$ ), and  $\chi(\omega) = k_{\text{str}}(\omega) / k_{\text{PZT}}$ , with  $k_{\text{PZT}}$  being the static stiffness of the PZT wafer active sensor. The electro-mechanical impedance method is applied by scanning a predetermined frequency range in the high kHz band and recording the complex impedance spectrum. During a frequency sweep, the real part of the E/M impedance,  $Z(\omega)$ , follows the up and down variation as the structural impedance as it goes through the peaks and valleys of the structural resonances and antiresonances (Giurgiutiu and Zagrai, 2002). By comparing the real part of the impedance spectra taken at various times during the service life of a structure, meaningful information can be extracted pertinent to structural degradation and the appearance of incipient damage. On the other hand, analysis of the impedance spectrum supplies important information about the sensor integrity. The frequency range used in the E/M impedance method must be high enough for the signal wavelength to be significantly smaller than the defect size. From this point of view, the high-frequency E/M impedance method differs organically from the low-frequency modal analysis approaches.

### Systematic E/M Impedance Analysis of Thin Circular Plates

A series of experiments on thin-gage circular plates were conducted to validate and calibrate the E/M impedance technique (Giurgiutiu and Zagrai, 2001). Twenty-five aluminum plate specimens (100-mm diameter, 1.6-mm thick) were constructed from aircraft-grade aluminum stock. Each plate was instrumented with one 7-mm diameter PZT active sensor placed at its center (Figure 12(b)).

#### E/M IMPEDANCE RESPONSE OF PRISTINE CIRCULAR PLATES

Theoretical analysis was conducted to understand and model the interaction between the plate and the active sensor, which is intimately bonded to the plate (Giurgiutiu and Zagrai, 2001). The circular-plate structure was modeled using a superposition of axisymmetric extensional and flexural modes:

$$u(r, t) = \left( \sum_k P_k R_k(r) \right) \cdot e^{i\omega t},$$

$$\frac{E}{\rho \cdot (1 - \nu^2)} \left( R_k''(r) + \frac{1}{r} R_k'(r) - \frac{1}{r^2} R_k(r) \right) = -\omega_k^2 \cdot R_k(r) \quad (8)$$

$$w(r, t) = \left[ \sum_m G_m \cdot Y_m(r) \right] \cdot e^{i\omega t},$$

$$D \cdot \nabla^4 Y_m(r) = \omega_m^2 \cdot \rho h \cdot Y_m(r) \quad (9)$$

where the mode shapes  $R_k(r)$  and  $Y_m(r)$  were expressed in terms of Bessel functions of the first kind and order 1 and 0, respectively:

$$R_k(r) = A_k J_1(\lambda_k r) \quad (10)$$

$$Y_m(r) = A_{m0} \cdot [J_0(\lambda_{m0} r) + C_{m0} \cdot I_0(\lambda_{m0} r)] \quad (11)$$

Hence, the pointwise structural stiffness presented to the piezoelectric wafer active sensor was deduced in the form:

$$k_{\text{str}}(\omega) = a^2 \rho \cdot \left[ \frac{2}{h} \cdot \sum_k \frac{[r_a R_k(r_a) + \int_0^{r_a} R_k(r) dr] R_k(r_a)}{(\omega_k^2 - 2i\zeta_k + \omega^2)} + \frac{h}{2} \cdot \sum_m \sum_n \frac{[Y_{mn}(r_a) - r_a \cdot Y_{mn}'(r_a)] \cdot Y_{mn}'(r_a)}{(\omega_{mn}^2 - 2i\zeta_{mn} + \omega^2)} \right]^{-1} \quad (12)$$

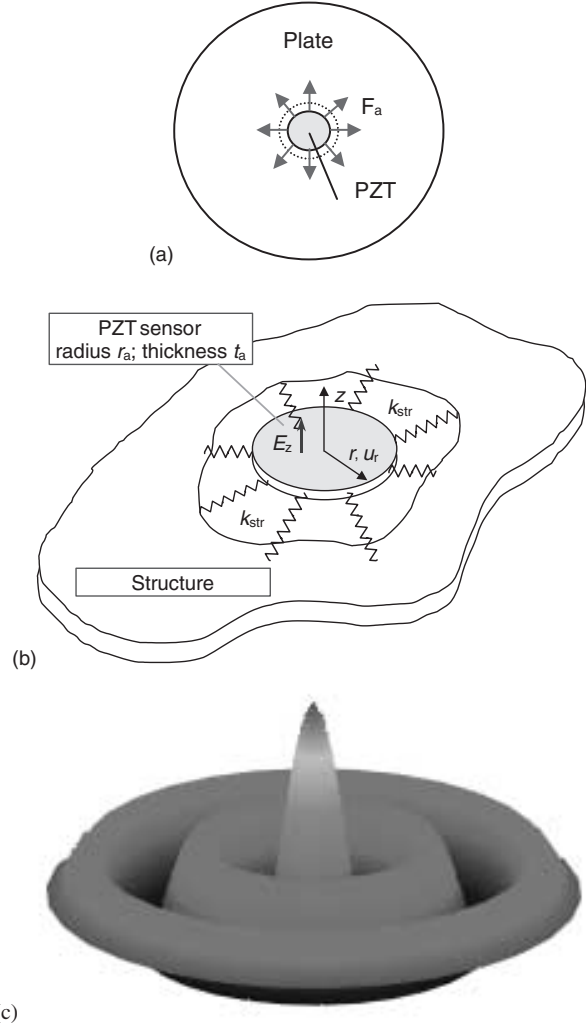


**Figure 13.** Analysis of a piezoelectric wafer active sensor: (a) Metallic plate instrumented with PZT wafer active sensor; (b) Interaction between structure and PZT wafer active sensor through the structural stiffness,  $k_{\text{str}}(\omega)$ ; (c) Third modeshape of the plate excited by the PZT wafer active sensor.

The PZT wafer active sensor was modeled using axisymmetric extensional modes and elastic-restrain boundary conditions that were imposed by the structural stiffness,  $k_{\text{str}}(\omega)$ , as shown in Figure 13. Hence, the sensor impedance,  $Z(\omega)$ , was expressed in the form

$$Z(\omega) = \left\{ i\omega C \left( 1 - k_p^2 \right) \left[ 1 + \frac{k_p^2}{1 - k_p^2} \frac{(1 + \nu) J_1(\varphi_a)}{\varphi_a J_0(\varphi) - (1 - \nu) J_1(\varphi_a) - \chi(\omega)(1 + \nu) J_1(\varphi_a)} \right] \right\}^{-1} \quad (13)$$

where  $\varphi_a = \omega r_a / c$ , while  $r_a$  is the radius of the PZT wafer,  $c = 1 / \sqrt{\rho s_{11}^E \cdot (1 - \nu_a^2)}$ , and  $k_p = (2d_{31}^E / [s_{11}^E \cdot (1 - \nu_a) \varepsilon_{33}^T])^2$  is the planar coupling factor. The ratio  $\chi(\omega) = k_{\text{str}}(\omega) / k_{\text{PZT}}$  represents the dynamic coupling between the sensor and the structure, with  $k_{\text{str}}(\omega)$  given by Equation (12) and  $k_{\text{PZT}} = t_a / [r_a s_{11}^E (1 - \nu)]$ .

Validation of the E/M impedance method was performed by measuring the E/M impedance response of instrumented 100-mm diameter plates and then comparing the results with the predictions made by

Equation (13). E/M impedance data was taken using an HP 4194A Impedance Analyzer. During the experiments, the specimens were supported on packing foam to simulate free-free boundary conditions. As shown in Figure 14, the results of this comparison were very good, giving confidence in E/M impedance method and its capability to sense the structural response at ultrasonic frequencies.

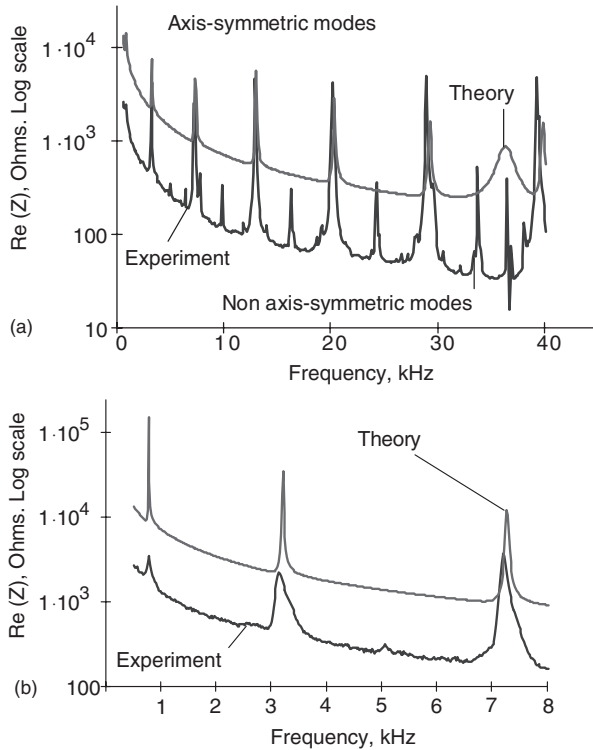


**Figure 14.** Experimental and calculated E/M impedance spectra for pristine plate specimen: (a) 0.5–40 kHz frequency range; (b) 0.5–8 kHz frequency range.

**DETECTION OF SEEDED CRACKS IN CIRCULAR-PLATE USING THE E/M IMPEDANCE RESPONSE**

A 10-mm circumferential EDM slit was used to simulate an in-service crack. The crack was placed at decreasing distance from the sensor (Figure 15). Thus, five groups with increasing amounts of damage were obtained. Group 0 represented the “pristine” condition, while Group 4 represented the condition with the severe damage. To permit evaluation of the statistical spread, each group contained five nominally identical specimens. During these experiments, very little statistical spread was observed. For illustration, Table 4 presents a summary of the results of the statistical analysis performed on the first four axisymmetric modes of the pristine plates (Group 0). Excellent frequency repeatability (1% standard deviation) was observed. Similar results were obtained for the “damage” specimens (Groups 1–4). Thus, confidence in the method’s repeatability and reproducibility was attained.

Damage detection experiments were conducted over three frequency bands: 10–40; 10–150, and 300–450 kHz.

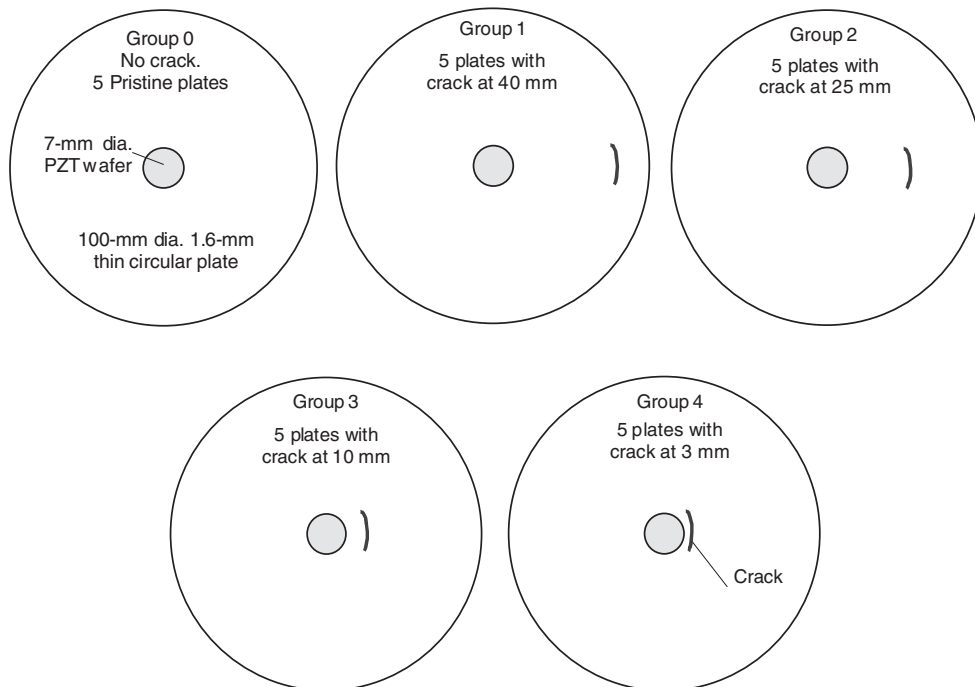


**Figure 15.** Systematic study of circular plates with simulated cracks (slits) at increasing distance from the E/M impedance sensor.

**Table 4. Statistical summary for resonance peaks of first four axisymmetric modes of a circular plate as measured with the piezoelectric active sensor using the E/M impedance method.**

Statistical Summary for Group 0 – Pristine			
Average Frequency (kHz)	Frequency STD, kHz (%)	Log <sub>10</sub> – Average Amplitude, Log <sub>10</sub> – Ohms	Log <sub>10</sub> – Amplitude STD, Log <sub>10</sub> – Ohms (%)
12.856	0.121 (1)	3.680	0.069 (1.8)
20.106	0.209 (1)	3.650	0.046 (1.2)
28.908	0.303 (1)	3.615	0.064 (1.7)
39.246	0.415 (1)	3.651	0.132 (3.6)

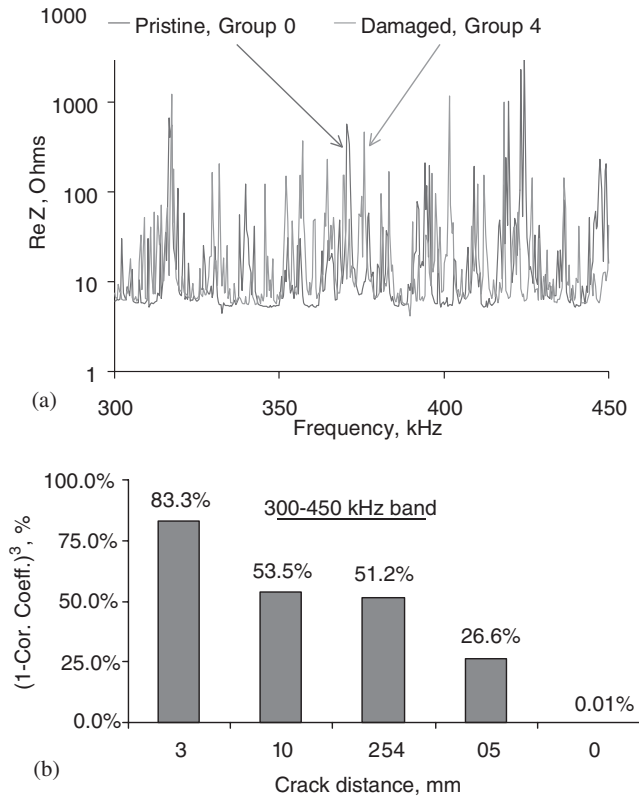


**Figure 16. E/M impedance results: (a) Superposed spectra of groups 1 & 5; (b) Variation of  $(1-R^2)^3$  damage metric with the distance between the crack and the sensor.**

The data was processed by analyzing the real part of the E/M impedance spectrum, and determining a damage metric to quantify the difference between two spectra, “pristine” and “damaged”. For illustration, Figure 16(a) indicates that the presence of the crack in the close proximity of the sensor drastically modifies the pointwise E/M impedance spectrum. Resonant frequency shifts and the appearance of new resonances are noticed. Several damage metrics were tried: root mean square deviation (RMSD); mean absolute percentage deviation (MAPD); covariance change (CC); correlation coefficient,  $R$ , deviation (CCD). The  $(1-R^2)^3$  damage metric was found to decrease almost linearly with the distance between the crack and the sensor (Figure 16(b)). However, in order to obtain consistent results in

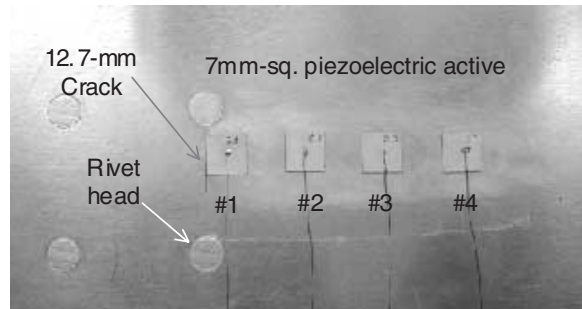


**Figure 17. Piezoelectric sensors installed on the aircraft panel with aging damage simulated by a 10-mm crack originating from a rivet.**

general situations, the proper frequency band (usually in high kHz) and the appropriate damage metric must be used. Further work is needed to investigate systematically the most appropriate damage metric algorithm that can be used for successful processing of the frequency spectra.

### E/M Impedance Experiments on Aging Aircraft Panels

Piezoelectric wafer active sensors were applied to the simulated aircraft panels to detect the change of E/M impedance spectrum induced by the proximity of a simulated crack. Figure 17 shows sensors installation: the sensors are placed along a line, perpendicular to a 12.7-mm crack originating at a rivet hole. The sensors are 7-mm square and are spaced at 7-mm pitch. E/M impedance readings were taken of each sensor in the 200–2600 kHz range. Figure 18(a) shows the real part of the E/M impedance spectrum. The spectrum reflects clearly defined resonances that are indicative of the coupled dynamics between the PZT sensors and the frequency-dependent pointwise structural stiffness as seen at each sensor location. The spectrum presented in Figure 18(a) shows high consistency. The dominant resonance peaks are in the same frequency range, and the variations from sensor to sensor are consistent with the variations previously observed in the circular plate experiments.

Examination of Figure 18(a) indicates that, out of the four E/M impedance spectra, that of sensor 1 (closest to the crack) has lower frequency peaks, which could

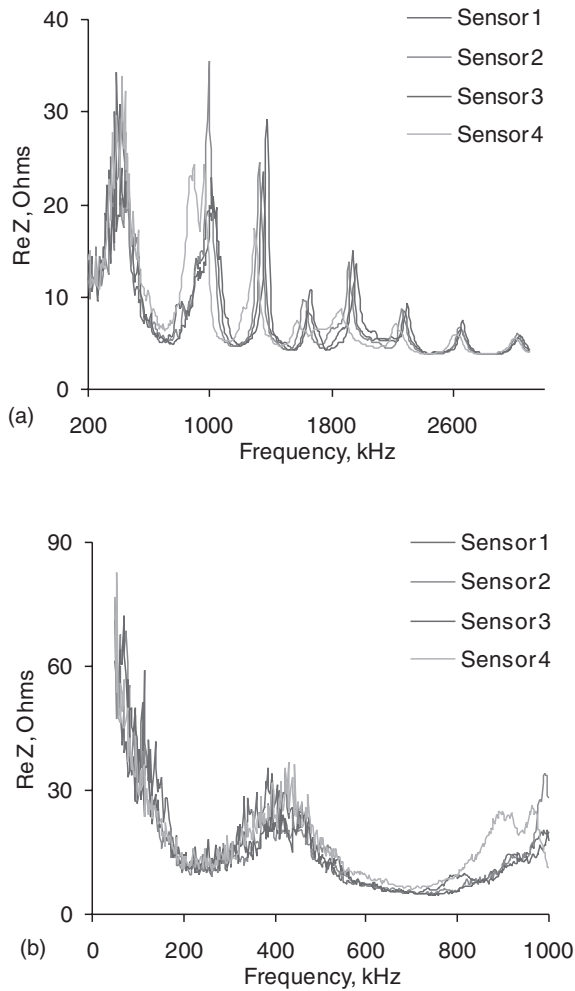


**Figure 18.** Real part of impedance for sensors bonded on aging aircraft structure: (a) 200–2600 kHz range; (b) Zoom into the 50–1000 kHz range.

be correlated to the presence of the damage. In order to better understand these aspects, further investigations were performed at lower frequencies, in the 50–1000 kHz range (Figure 18(b)). In this range, we can see that the crack presence generated features in the sensor #1 spectrum that did not appear in the other sensors spectra. For example, sensor #1 presents an additional frequency peak at 114 kHz that is not present in the other sensors. It also shows a downward shift of the 400 kHz main peak. These features are indicative of a correlation between the particularities of sensor #1 spectrum and the fact that sensor #1 is placed closest to the crack. However, at this stage of the investigation, these correlations are not self evident, nor are they supported by theoretical analysis and predictive modeling of the structure under consideration. Further signal processing and features extraction improvements are needed to fully understand the correlation between the spectral features of the E/M impedance response and the presence of structural damage in the sensor vicinity.

Based on these results, we formulated a damage detection strategy to be used with the E/M impedance method. The real part of the E/M impedance ( $\text{Re } Z$ ) reflects the pointwise mechanical impedance of the structure, and the E/M impedance spectrum is equivalent to the pointwise frequency response of the structure. As damage (cracks, corrosion) develops in the structure, the pointwise impedance in the damage vicinity changes. Piezoelectric active sensors placed at critical structural locations detect these near-field changes. In addition, due to the sensing localization property of this method, far-field influences will not be registered in the E/M impedance spectrum. The integrity of the sensor itself, which may also modify the E/M impedance spectrum, is independently confirmed using the imaginary part of E/M impedance ( $\text{Im } Z$ ), which is highly sensitive to sensor disbond, but much less sensitive than the real part to structural resonances (Giurgiutiu and Zagrai, 2002).

## SUMMARY AND CONCLUSIONS

Piezoelectric-wafer active sensors are small inexpensive nonintrusive sensors that can be applied on existing aging aircraft structures to monitor the onset and progress of structural damage (cracks and corrosion). Two complementary methods can be simultaneously used with the same active-sensor installation: (a) elastic wave propagation; and (b) electro-mechanical (E/M) impedance. Through systematically conducted experiments, this paper has attained a double objective: (a) to develop and validate the methodology using simple-geometry specimens; and (b) to illustrate its practical application using realistic structural specimens representative of aging aerospace structures with seeded crack and corrosion.

Elastic wave propagation was studied for far-field damage detection. Simple-geometry specimens were used to clarify the Lamb wave propagation mechanism, verify the group-velocity dispersion curves, and illustrate the pulse-echo method using the reflections from the specimen boundaries. Realistic aging-aircraft specimens were used to demonstrate how a 12.7-mm crack emanating from a rivet hole can be detected with the pulse-echo method using a 300 kHz wave generated and received by the same piezoelectric-wafer active sensor placed at 100 mm from the crack. Acoustic emission (AE) and low-velocity impact were also detected. The high sensitivity of these sensors is remarkable: AE signals of up to  $\pm 0.5$  V were directly recorded without the need for any signal conditioning/pre-amplifiers. For low velocity impact, the corresponding values were  $\pm 1.5$  V. Impact location was detected with 0.2% accuracy in the  $x$  direction, and 6.2% in the  $y$  direction.

The E/M impedance method was used for near-field damage detection. The E/M impedance experiments showed that the real part of the E/M impedance spectrum is clearly influenced by the presence of damage (simulated crack). This behavior was explained in terms of the direct correlation between the pointwise dynamic stiffness of the structure at the sensor location and the real part of the E/M impedance measured at the sensor terminals. Experiments performed on 100-mm diameter thin-gage circular plates showed that the distance between sensor and a simulated crack can be directly correlated with the  $(1-R^2)^3$  damage metric. Experiments performed on realistic aging aircraft panel showed that a left shift in the natural frequencies and the appearance of a new frequency peak at around 114 kHz were created by the presence of a 12.7-mm crack in the sensor proximity. However, the complete understanding of the relationship between the sensor location and the changes in the E/M spectrum for complex built-up panels has not yet been fully achieved. Additional efforts in advanced signal processing, identification of spectrum features that are sensitive to the crack presence, and adequate modeling and simulation are required.

This study has shown that the E/M impedance method and the wave propagation approach are complementary techniques that can be simultaneously used for damage detection in aging aircraft structures instrumented with an array of piezoelectric-wafer active sensors. Since one method works in the near field, while the other acts in the far field, their simultaneous utilization will ensure that the aging aircraft structure is fully covered during the health monitoring process.

## ACKNOWLEDGMENTS

Financial support of US DOE through the Sandia National Laboratories, contract doc. # BF 0133. Sandia National Laboratories is a multiprogram laboratory operated by Sandia Corporation, a Lockheed Martin Company, for the US DOE, contract DE-AC04-94AL85000.

## REFERENCES

- Bartkowicz, T.J., Kim, H.M., Zimmerman, D.C. and Weaver-Smith, S. 1996. "Autonomous Structural Health Monitoring System: A Demonstration," In: *Proceedings of the 37th AIAA/ASME/ASCE/AHS/ASC Structures, Structural Dynamics, and Materials Conference*, Salt-Lake City, UT, April 15–17.
- Blanas, P., Wenger, M.P., Shuford, R.J. and Das-Gupta, D.K. 1997. "Active Composite Materials and Damage Monitoring," In: *Proceedings of the International Workshop on Structural Health Monitoring*, Stanford University, CA, September 18–20 pp. 199–207.
- Blitz, J. and Simpson, G. 1996. *Ultrasonic Methods of Non-Destructive Testing*, Chapman & Hall, New York.
- Boller, C., Biemans, C., Staszewski, W., Worden, K. and Tomlinson, G. 1999. "Structural Damage Monitoring Based on an Actuator-Sensor System," In: *Proceedings of SPIE Smart Structures and Integrated Systems Conference*, Newport CA, March 1–4.
- Cawley, P. 1984. "The Impedance Method for Non-Destructive Inspection," *NDT International*, 17(2):59–65.
- Chang, F.-K. 1995. "Built-In Damage Diagnostics for Composite Structures," In: *Proceedings of the 10th International Conference on Composite Structures (ICCM-10)*, Vol. 5, Whistler, B.C., Canada, August 14–18, pp. 283–289.
- Chang, F.-K. 1998. "Manufacturing and Design of Built-in Diagnostics for Composite Structures," *52nd Meeting of the Society for Machinery Failure Prevention Technology*, Virginia Beach, VA, March 30–April 3.
- Chang, F.-K. 2001. "Structural Health Monitoring: Aerospace Assessment," *Aero Mat 2001, 12th ASM Annual Advanced Aerospace Materials and Processes Conference*, 12–13 June 2001, Long Beach, CA.
- Duke, J.C. Jr. 1988. *Acousto-Ultrasonics – Theory and Applications*, Plenum Press, New York.
- Dupont, M., Osmont, R., Gouyon, R. and Balageas, D.L. 2000. "Permanent Monitoring of Damage Impacts by a Piezoelectric Sensor Based Integrated System," In: *Structural Health Monitoring 2000*, pp. 561–570, Technomic-CRC Press, Boca Raton.
- Dzenis, Y. and Qian, J. 2001. "Analysis of Microdamage Evolution Histories in Composites," *7th ASME NDE Topical Conference*, San Antonio, TX, April 23–25.
- Farrar, C.R., Sohn, H., Fugate, M.L. and Czarnecki, J.J. 2001. "Integrated Structural Health Monitoring," In: *Proceeding of SPIE Conference on Advanced Nondestructive Evaluation for Structural and Biological Health Monitoring*, Vol. 4335, March 6–8, 2001, Newport Beach, CA, pp. 1–8.
- Giurgiutiu, V. and Rogers, C.A. 1997. "Electro-Mechanical (E/M) Impedance Method for Structural Health Monitoring in a Non-Destructive Evaluation," *Int. Workshop on Structural Health Monitoring*, Stanford University, CA, Sep. 18–20, pp. 433–444.
- Giurgiutiu, V. and Zagrai, A. 2001. "Electro-Mechanical Impedance Method for Crack Detection in Thin Plates," *Journal of Intelligent Material Systems and Structures*, 12(10):709–718.
- Giurgiutiu, V. and Zagrai, A. 2002. "Embedded Self-Sensing Piezoelectric Active Sensors for On-Line Structural Identification," *ASME Journal of Vibration and Acoustics*, 124:116–125.
- Giurgiutiu, V., Bao, J. and Zhao, W. (2001) "Active Sensor Wave Propagation Health Monitoring of Beam and Plate Structures," *SPIE's 8th Annual International Symposium on Smart Structures and Materials*, 4–8 March 2001, Newport Beach, CA, paper #4327–32, pp. 234–245.
- Goldin, D.S., Venneri, S.L. and Noor, A.K. 2001. "Fresh Air, Wide-open Space," *Mechanical Engineering*, pp. 48–55.
- Ikegami, R. and Haugse, E.D. 2001. "Structural Health Management for Aging Aircraft," In: *Proceedings of SPIE Industrial and Commercial Applications of Smart Structures Technologies*, Vol. 4332, pp. 60–67.
- Krautkramer, J. and Krautkramer, H. 1990. *Ultrasonic Testing of Materials*, Springer-Verlag, New York.
- Lange, N. 1978. "Characteristics of the Impedance Method of Inspection and of Impedance Inspection Transducers," *Sov. J. NDT*, 958–966.
- Lemistre, M., Gouyon, R., Kaczmarek, H. and Balageas, D. 1999. "Damage Localization in Composite Plates Using Wavelet Transform Processing on Lamb Wave Signals," *2nd International Workshop of Structural Health Monitoring*, Stanford University, September 8–10, pp. 861–870.
- Mal, A. 2001. "NDE for Health Monitoring of Aircraft and Aerospace Structures," In: *Proceeding of the 7th ASME NDE Topical Conference*, NDE-Vol. 20, pp. 149–155.

- Rose, J.L. 1999. *Ultrasonic Waves in Solid Media*, Cambridge University Press, New York.
- Rose, J.L. 2001. "A Vision of Ultrasonic Guided Wave Inspection Potential," In: *Proceeding of the 7th ASME NDE Topical Conference*, NDE-Vol. 20, pp. 1–5.
- Staveley NDT Technologies 1998. "Sonic Bondmaster™ Product Description," Kennewick, WA 99336.
- Viktorov, I.A. 1967. *Rayleigh and Lamb Waves*, Plenum Press, New York.
- Wang, C.S. and Chang, F.-K. 2000. "Built-In Diagnostics for Impact Damage Identification of Composite Structures," In: Fu-Kuo Chang (ed.), *Structural Health Monitoring 2000*, pp. 612–621, Technomic-CRC Press, Boca Raton.